# Photocatalytic and photoluminescent properties of a system based on SmPO4 nanostructure phase

A. Bouddouch, E. Amaterz, A. Taoufyq, B. Bakiz, F. Guinneton, Sylvie Villain, J.C. Valmalette, J.R. Gavarri, A. Benlhachemi

Available online at www.sciencedirect.com

ScienceDirect

materialstoday: PROCEEDINGS

ELSEVIER

**ICMES_2019**

# Photocatalytic and photoluminescent properties of a system based on $SmPO_4$ nanostructure phase

A. Bouddouch[a, b], E. Amaterz[a, c], A. Taoufyq[a], B. Bakiz[a], F. Guinneton[b], S. Villain[b], J. C. Valmalette[b], J.R. Gavarri[b], A. Benlhachemi[a]

[a]*Laboratoire Matériaux et Environnement (LME), Faculté des Sciences, Université Ibn Zohr, B.P 8106, Cité Dakhla, Agadir, Maroc.*
[b]*Institut Matériaux Microélectronique et Nanosciences de Provence, Université de Toulon, Aix Marseille Univ, CNRS, IM2NP, Toulon, France.*
[c]*Institut de Thermique, Mécanique, Matériaux (ITHEMM), Université de Reims ChampagneArdenne, Reims, France.*

**Abstract**

In the present work, we investigate the structural, microstructural, vibrational, photocatalytic and luminescence properties of the system $SmPO_4$ thermally treated at 900 °C. Polycrystalline sample was elaborated using a coprecipitation method. The sample was then characterized using different techniques such as X-ray diffraction, Scanning electron microscopy, Infrared spectroscopy, Raman spectroscopy and photoluminescence analysis under UV excitation. X-ray diffraction profile analysis showed that the pure monoclinic phase $P2_1/n$ was observed. The scanning electron microscopy experiments showed a homogeneous distribution of morphologies and indicated that $SmPO_4$ was in nano-sized particle. Attributions of Raman and FTIR vibrational modes were proposed. For the photocatalytic activity, UV-visible spectrophotometer has been used to analyze the evolution of photodegradation of rhodamine B (RhB). The photocatalytic degradation of rhodamine B in the presence of $SmPO_4$ photocatalyst has been studied for the first time. Photoluminescence (PL) properties of $SmPO_4$ nanoparticle under UV excitation has been reported and investigated.

***Keywords****: Samarium phosphate $SmPO_4$; co-precipitation method; spectroscopy methods; Luminescence properties; photocatalytic activity.*

## 1. Introduction

In the general framework of environmental protection and energy savings, recent developments of new materials for photocatalysis or photoluminescence applications have emerged in various industrial fields such as radiation sensors, light emitting diodes (LED), artificial lights, X-ray medical radiography, display devices, lasers and luminescent markers for biomedicine [1–9]. In this context, various systems have been developed in recent years including vanadates [10–12], oxides [13–15], hydroxides [16,17], tungstates [18–20], molybdates [21] and phosphates [22–28]. Recent studies on solid solutions of tungstate and molybdate materials [21,29] showed that the photoluminescence under UV and X-ray excitations depended on substitution level, thermal treatments and crystal growth or morphologies. All emitted signals were linked to modifications of charge transfers in $WO_4$ or $MoO_4$ groups due to substitution.

In the present study, we deal with samarium phosphate $SmPO_4$, well-known for specific photoluminescent properties in presence or not of doping elements, for example by $Eu^{3+}$ [30], $Tb^{3+}$ [31], $Gd^{3+}$ [32]. It should be noted that this material was involved in other applications, as a catalyst [33], ion cathode material [34], in magnetic resonance and bio-optical imaging [32].

Concerning the structure [35], samarium phosphate crystallizes in the monoclinic system conforming to space group $P2_1/n$ (No. 14, Z = 4). The lattice parameters of the compound are as follows: a = 6.669(l), b = 6.868(2), c = 6.351(l) Å and β = 103.92(2).

For the preparation of this phase, several routes were already used such as hydrothermal reaction [30], sol gel synthesis [36], solid-state process [37] and sometimes the co-precipitation method [38,39]. However, little work has been reported on photoluminescence and photocatalytic properties of samarium phosphate to our knowledge. In this letter, we present the research work on these properties of $SmPO_4$ nano system obtained by co-precipitation method.

## 2. Experimental section

### *2.1. Preparation of powders*

The synthesis of samarium phosphate was carried out by the coprecipitation method in an aqueous medium.

**Solution A**: 2 g of $Sm(NO_3)_3.6H_2O$ (Sigma-Aldrich ≥ 99.0%) were dissolved in 50 ml of distillated water. The mixture was stirred for 30 minutes at room temperature.

**Solution B:** 0.5176 g of ammonium hydrogen phosphate $(NH_4)H_2PO_4$ (Pro Labo ≥ 98.0%) were dissolved in 50 ml of distillated water. The mixture was stirred for 30 minutes at room temperature.

Then, solution B was added dropwise to the solution A, with stirring for 30 min, the pH was maintained to the value 9.5 by the addition of ammonium hydroxide ($NH_4OH$) to confirm the total formation of the precipitate. The set was maintained under agitation at ambient temperature, for a duration of maturation $t_m$ = 30 min.

The obtained precipitate was filtered under vacuum and washed several times by the distilled water and the pure ethanol to eliminate the $NH_4^+$ and $NO_3^-$ ions, then the obtained filtrate was dried in the oven for a night at 70 °C and calcined at 900 °C for three hours.

### *2.2 Characterization techniques*

The identification of the crystalline phase of powder was carried out using X-ray diffraction (XRD). The XRD pattern of the polycrystalline sample was recorded at room temperature using an Empyrean Panalytical diffractometer operating at 45 kV/35 mA, using the $CuK(\alpha_1-\alpha_2)$ radiation ($\lambda$ = 1.5406 and 1.5444 Å) of copper source with Ni filter, and working in continuous mode with a step size of 0.013°.

The identification of the phase was firstly obtained from the classical Powder Diffraction File database, then, cell parameters were refined making use of the Param software. Scanning electron microscopy (SEM) analysis was used to observe the morphology and the local composition of the crystalline phase. The device used was a Supra 40 VP Column Gemini Zeiss operated at 20 KeV, coupled with an Energy Dispersive X-rays Spectroscopy (EDXS) type analyzer, allowing the determination of the local elemental compositions of our material.

Fourier transformed infrared spectroscopy (FTIR) analysis was used to characterize the vibration modes and complete the identification of the simple. The FTIR-ATR characterizations were carried out using a Shimadzu spectrometer equipped with a Jasco ATR PRO ONE module. The sample was scanned in transmission mode in the 450-4000 $cm^{-1}$ wavenumber range, with a step of 4 $cm^{-1}$. Raman spectroscopy was used to correlate the vibrational characteristics with the structural analysis from X-ray diffraction. The Raman spectrum was registered at room temperature using spectrometer Horiba Jobin-Yvon HR800 LabRam system, with wavenumbers of Raman shifts ranging between 50 and 1500 $cm^{-1}$. The 633 nm line of an Ar-ion laser was used as the excitation source; the photonic power applied to the samples was limited to 5 µW with an acquisition time of 30 s.

### *2.3. Photocatalysis procedure*

The photocatalytic activity of the photocatalyst was evaluated by the photocatalytic degradation of rhodamine B, in an aqueous medium. Each powder (mass of 100 mg) was suspended in 100 mL of pollutant solution (5 mg/L). Before irradiation, the solution was stirred for one hour inside the reactor to get the adsorption-desorption equilibrium between the support and dye. During irradiation, 3 mL solution was collected at time intervals of one hour. UV visible JENWAY-6705 spectrophotometer was used to determine the concentration of rhodamine B as a function of irradiation time. . The degradation percentage was calculated using the expression:

$$I(t) = 100*C_0\text{-}C_t/C_0 \quad \text{Eq. 1}$$

Where $C_0$ and $C_t$ are the initial concentrations and concentrations at time t of irradiation, respectively.

*2.4. Photoluminescence experiments*

The device used to perform photoluminescence (PL) tests under UV excitation was a Horiba Jobin-Yvon HR800 LabRam spectrometer equipped with an argon ionized laser as a source of excitement with a wavelength of 364 nm (3.4 eV) and a power fixed at 5 μW. The entrance slit, positioned behind the filter, is a diaphragm with a diameter variable between 50 to 500 mm. The exposed polycrystalline sample is obtained by compression on a glass slide. The irradiated zone was limited to 1 mm in diameter for all samples. The spherical mirror, characterized by an 800 mm focal length, allows revealing the scattered radiation from the input to the dispersive grating to obtain a spectra slot. The measurements were recorded in the spectral range between 500 and 750 nm with an acquisition time of 5 seconds.

## 3. Results and discussions

*3.1. X-ray diffraction: structural study*

Figure 1 shows the obtained pattern of samarium phosphate $SmPO_4$ and in the 2θ angle range 10 to 80 deg. In this figure, the X-ray diffraction pattern is characteristic of the stabilization of the expected phase as the calcination was at 900 °C. The XRD result exhibited that the as-synthesized $SmPO_4$ nanoparticle is of single phase with a monoclinic structure.

The crystal cell parameters of the samarium phosphate phase was refined and the results are presented in Table 1. These parameters are in quite good agreement with the literature data.

The nanocrystalline size of the sample of the monoclinic phase can be roughly estimated from the Scherrer equation, $D=0{,}941\lambda/\beta\cos(\theta)$, where D is the average grain size, λ is the X-ray wavelength (0.15405 nm), θ and β are the diffraction angle and full-width at half-maximum (FWHM) of an observed peak. The strongest peak (-112) at 31.72° of the monoclinic phase were used to calculate the average crystallite size (D). The estimated average crystallite size are 39.3 nm for $SmPO_4$ sample.

Fig. 1. XRD pattern of samarium phosphate $SmPO_4$ calcined at 900 °C.

Table 1. Refined cell parameters and cell volumes of samarium phosphate crystal lattice.

*3.2. Scanning electron microscopy: morphological study*

The morphology of the $SmPO_4$ sample obtained from SEM is shown in Figure 2 abcd. In Fig. 2a, small crystallite sizes ranging between 60 to 120 nm are observed. In Fig. 2b, c and d, inhomogeneous distribution is seen.

The EDX local microanalysis presented in Figure 3e was performed to determine the composition of sample. EDX microanalysis reports the analysis for each sample: the Sm/P ratio is found to range between 0.99 and 1.2.

Fig. 2. SEM images and EDX spectrum of samarium phosphate $SmPO_4$ treated at 900 °C.

*3.3. Fourier transformed infrared analysis*

The FTIR spectrum of $SmPO_4$ calcined at 900 °C is show in figure 3. The FTIR bands of sample is attributed according to the bibliography [30]. The spectrum show the apparition of the bands corresponding to the different vibrations of the $PO_4^{3-}$ phosphate groups in the frequency range 500-650 $cm^{-1}$ and 950-1150 $cm^{-1}$ (Fig. 3b). In detail, the peaks centered at 952, 985, 1045, and 1149 $cm^{-1}$, which are related to the P-O stretching vibrations ($\nu_3$ and $\nu_1$) of $PO_4^{-3}$. There are various IR bands below 670 $cm^{-1}$ that correspond to antisymmetric and symmetric bending modes of P-O-P and O-P-O, which are difficult to be distinguished, but there are two weak intensity peaks of 622 and 540 $cm^{-1}$, which are well known $\nu_3$ stretching and $\nu_4$ bending O-P-O vibrations of the $PO_4^{-3}$ phosphate group, respectively. The two peaks observed at 1654 $cm^{-1}$ and 3446 $cm^{-1}$ are assigned to the deformation and elongation vibrations of OH, respectively (Fig. 3a) [40]. Which is attributed to O-H stretching vibrations of adsorbed surface water molecules.

Fig. 3. FTIR spectrum of $SmPO_4$ nanoparticle between (a) 400-4000 and (b) 400-1400 $cm^{-1}$.

*3.4. Raman spectroscopy study*

Figure 4 reports the Raman spectrum corresponding to the $SmPO_4$ nanoparticle. From the literature data [41], the three bands observed at 1084, 1050 and 980 $cm^{-1}$ in the spectrum of the as-prepared sample correspond to the antisymmetric and symmetric stretching vibrations of P–O band. the Raman bands observed between 400-720 $cm^{-1}$, more precisely at 405, 467, 548, 628 and 719 $cm^{-1}$, can be assigned to bending modes of $PO_4$ units, from which 628 and 548 $cm^{-1}$ vibrations are the antisymmetric ones while 467 and 405 $cm^{-1}$ vibrations are the symmetric ones. These results confirm the observations of the IR study. The two bands observed at 78 and 204 $cm^{-1}$ are generally attributed to vibrations involving the movement of cations and tetrahedron units.

Fig. 4. Raman spectrum of $SmPO_4$ sample.

## 4. Photocatalysis study

In this environmental application, we study the photocatalytic degradation of rhodamine B, by following the evolution, over time, of the characteristic absorption band of this pollutant, whose maximum is located at the wavelength $\lambda_{max}$ = 554 nm. In other words, the photodegradation was characterized by the variation with the time t of the intensity of the RhB absorption band. This variation is reported by the ratio $C_t/C_O$, $C_t$ being proportional to the RhB concentration at time t and $C_0$ being the initial concentration of this pollutant, after one hour of the absorption-desorption process in the solution.

In the absence of catalyst and under UV irradiation, photodegradation did not exceed 41% of the initial amount of Rhodamine B for 8 hours. This is due to the direct photolysis process (Figure 5a).

Figure 5b shows the reduction of the maximum absorption band of this pollutant as a function of UV irradiation time. Figure 5c shows the kinetics of photocatalytic degradation in the presence of photocatalyst. After 8 hours of UV irradiation, the degradation efficiency I(t) determined from eq. 1 is found to be 96%.

The plots of $\ln(C_0/C_t)$ versus t are shown in Fig. 5d. In the case of a first order kinetics rate law (Langmuir–Hinshelwood model),[42] the ratio $C_t/C_0$ can be expressed as follows:

$$\text{Ln}\ (C_t/C_0) = -\ k_{obs}\ t \quad \text{Eq.2}$$

Where the kinetics constant $k_{obs}$ (depending on RhB concentration and temperature of solution) characterize the photocatalytic efficiency. As shown in Fig. 5d, the Langmuir–Hinshelwood kinetic equation fits quite well with the experimental data and with a constant $k_{obs}$ of the order of 0.3865 $h^{-1}$ (correlation coefficient $R^2 > 0.97$), indicating the applicability of the Langmuir–Hinshelwood kinetic model.

Fig. 5. (a) stability of the rhodamine B under UV light, (b) UV–vis absorption with time irradiation of a solution containing 100 mg $SmPO_4$ and a 5ppm of RhB, (c) Photodegradation of RhB in SmP suspension under UV-visible light (initial concentration of RhB, 5 mg/L). (d) pseudo-first-order kinetics of the photocatalyst.

## 5. Photoluminescence study

The photoluminescence spectrum of samarium phosphate nanoparticle, obtained under UV excitation ($\lambda_{ex}$ =363.8 nm) are shown in Figure 6. The emission spectra were processed using Labspec program. Most studies in the literature of this system confirm that the emission bands observed from $SmPO_4$ are ascribed to the transitions from $^4G_{5/2}$ excited state to $^6H_{J/2}$ (J¼ 5, 7, 9 and 11) ground states of $Sm^{3+}$. The characteristic $Sm^{3+}$ emissions in the $SmPO_4$ nanopowder consist of four main orange-red emission bands [43].

The detailed analysis of the emission bands and variations of PL intensities reveal that:

The strongest emission peak at 596 nm originates from the typical $^4G_{5/2}$ -$^6H_{7/2}$ transition of $Sm^{3+}$, the other emission peaks at 559 nm, 642 nm and 701 nm are attributed to the transitions $^4G_{5/2}$-$^6H_{5/2}$, $^4G_{5/2}$-$^6H_{9/2}$ and $^4G_{5/2}$-$^6H_{11/2}$ transitions of $Sm^{3+}$, respectively [44,45]. In short, the intensity of transitions f-f indicates that, for this material, excitation at 363.8 nm generates a high emission of 597 nm, making it a promising luminophores emitting orange-reddish colors for white LED applications. It is worth to mention that the photoluminescent results are in a good correlation with those of photocatalysis, indeed, the best photocatalyst has shown low photoluminescence response as a reason of the non-recombination of the electron-hole pairs.

Fig. 6. Experimental emission bands of the $SmPO_4$ polycrystalline phase.

## 6. Conclusion

In conclusion, the samarium phosphate nanostructure was prepared by co-precipitation process. The XRD pattern of the material exhibited a monoclinic-crystal structure with a space group $P2_1/n$. The SEM analysis shows a nanocrystalline sizes with dimensions between 60 to 120 nm. The degradation associated with the $SmPO_4$ catalyst towards the RhB pollutant as a model dye is average with a photocatalytic efficiency of the order of 96.6% after 8 hours of irradiation under UV-visible. For the photoluminescence test, the $SmPO_4$ shows strong orange–red luminescence. More precisely, the strongest emission intensity was observed for the $^4G_{5/2} \rightarrow {}^6H_{7/2}$ (596 nm) transition of the $Sm^{3+}$ ions with the 363.8 nm excitation. Finally, this work will motivate new developments in both orthophosphate materials, photoluminescence and photocatalytic methodology under UV-Visible light irradiation.


## Acknowledgements

This work was carried out in the laboratory materials and environment (LME), at the faculty of sciences Agadir, Ibn Zohr University, IM2NP laboratory, University of Toulon and financially supported by CAMPUS FRANCE (PHC TOUBKAL 2018 (French-Morocco bilateral program) Grant Number: 38999WE) and PPR project financed by the CNRST under number PPR/2015/32.


## References


[1] G. Boulon, Luminescence des ions activateurs dans les matériaux inorganiques et applications, Rev. Phys. Appliquée. 21 (1986) 689–707. doi:10.1051/rphysap:019860021011068900.

[2] W. Wang, P. Yang, Z. Cheng, Z. Hou, C. Li, J. Lin, Patterning of red, green, and blue luminescent films based on CaWO 4:Eu3+, CaWO4:Tb3+, and CaWO 4 phosphors via microcontact printing route, ACS Appl. Mater. Interfaces. 3 (2011) 3921–3928. doi:10.1021/am2008008.

[3] M.G. Kwak, J.H. Park, S.H. Shon, Synthesis and properties of luminescent Y2O3:Eu (15–25 wt%) nanocrystals, Solid State Commun. 130 (2004) 199–201. doi:10.1016/j.ssc.2004.01.042.

[4] A. Karthikeyani, R. Jagannathan, Eu2+ luminescence in stillwellite-type SrBPO5- a new potential X-ray storage phosphor, J. Lumin. 86 (2000) 79–85. doi:10.1093/carcin/15.7.1399.

[5] E. Ishow, A. Brosseau, G. Clavier, K. Nakatani, P. Tauc, C. Fiorini-Debuisschert, S. Neveu, O. Sandre, A. Leaustic, Multicolor Emission of Small Molecule-Based Amorphous Thin Films and Nanoparticles with a Single Excitation Wavelength, Chem. Mater. 20 (2008) 6597–6599.

[6] J.R. O'Connor, Unusual crystal-field energy levels and efficient laser properties of YVO4:Nd, Appl. Phys. Lett. 9 (1966) 407–409. doi:10.1063/1.1754631.

[7] E.L. Cates, S.L. Chinnapongse, J.-H. Kim, J.-H. Kim, Engineering Light: Advances in Wavelength Conversion Materials for Energy and Environmental Technologies, Environ. Sci. Technol. 46 (2012) 12316–12328. doi:\url{10.1021/es303612p}.

[8] D.K. Chatterjee, M.K. Gnanasammandhan, Y. Zhang, Small upconverting fluorescent nanoparticles for biomedical applications, Small. 6 (2010) 2781–2795. doi:10.1002/smll.201000418.

[9] F. Wang, W.B. Tan, Y. Zhang, X. Fan, M. Wang, Luminescent nanomaterials for biological labelling, Nanotechnology. 17 (2006) R1–R13. doi:10.1088/0957-4484/17/1/R01.

[10] A. Huignard, T. Gacoin, J. Boilot, Synthesis and Luminescence Properties of Colloidal YVO4:Eu Phosphors Arnaud, Chem. Mater. 12 (2000) 1090–1094. doi:10.1021/cm990722t.

[11] K. Riwotzki, M. Haase, Colloidal YVO4 : Eu and YP0.95V0.05O4 : Eu Nanoparticles : Luminescence and

Energy Transfer Processes, J. Phys. Chem. B. 105 (2001) 12709–12713.

[12] S. Obregón, G. Colón, Heterostructured Er3+doped BiVO4with exceptional photocatalytic performance by cooperative electronic and luminescence sensitization mechanism, Appl. Catal. B Environ. 158–159 (2014) 242–249. doi:10.1016/j.apcatb.2014.04.029.

[13] T. Jan, S. Azmat, B. Wahid, M. Adil, H. Alawadhi, Q. Mansoor, Z. Farooq, S.Z. Ilyas, I. Ahmad, M. Ismail, Chemically synthesized ZnO-Bi2O3(BZO) nanocomposites with tunable optical, photoluminescence and antibacterial characteristics, Mater. Sci. Semicond. Process. 84 (2018) 71–75. doi:10.1016/j.mssp.2018.05.007.

[14] N. Bao, Y. Liu, Z.W. Li, H. Yu, H.T. Bai, L. Xia, D.W. Feng, H.B. Zhang, X.T. Dong, T.Y. Wang, J. Han, R.Y. Wu, Q. Zhang, Construction of order mesoporous (Eu-La)/ZnO composite material and its luminescent characters, J. Lumin. 177 (2016) 409–415. doi:10.1016/j.jlumin.2016.05.025.

[15] M. Ajmal, T. Ali, S. Ahmad Mian, M. Adil Khan, S. Ahmad, A. Ali Khan, Effects of Ce3+-doping concentration on the luminescent properties of La2O3:Ce3+phosphors, Mater. Today Proc. 4 (2017) 4924–4929. doi:10.1016/j.matpr.2017.04.097.

[16] A.A. Ansari, A. Aldalbahi, J.P. Labis, A.M. El-Toni, M. Ahamed, M.A. Manthrammel, Highly biocompatible, monodispersed and mesoporous La(OH)3:Eu@mSiO2core-shell nanospheres: Synthesis and luminescent properties, Colloids Surfaces B Biointerfaces. 163 (2018) 133–139. doi:10.1016/j.colsurfb.2017.12.026.

[17] A. García-Murillo, F. de J.Carrillo-Romo, J. Oliva-Uc, T. A.Esquivel-Castro, S. Díaz de la Torre, Effects of Eu content on the luminescent properties of Y2O3:Eu3+ aerogels and Y(OH)3 Y2O3:Eu3+@SiO2 glassy aerogels, Ceram. Int. J. 43 (2017) 12196–12204. doi:10.1016/j.ceramint.2017.06.079.

[18] A. Taoufyq, V. Mauroy, F. Guinneton, B. Bakiz, S. Villain, A. Hallaoui, A. Benlhachemi, G. Nolibe, A. Lyoussi, J.R. Gavarri, Role of the chemical substitution on the luminescence properties of solid solutions Ca(1-x)Cd(x)WO4 ($0 \leq x \leq 1$), Mater. Res. Bull. 70 (2015) 40–46. doi:10.1016/j.materresbull.2015.04.006.

[19] H. Ait Ahsaine, M. Ezahri, A. Benlhachemi, B. Bakiz, S. Villain, J.C. Valmalette, F. Guinneton, M. Arab, J.R. Gavarri, Structural, vibrational study and UV photoluminescence properties of the system Bi(2-x)Lu(x)WO6 ($0.1 \leq x \leq 1$), RSC Adv. 5 (2015) 96242–96252. doi:10.1039/c5ra19424e.

[20] B. Bakiz, A. Hallaoui, A. Taoufyq, A. Benlhachemi, F. Guinneton, S. Villain, M. Ezahri, J.C. Valmalette, M. Arab, J.R. Gavarri, Luminescent properties under X-ray excitation of Ba(1−x)PbxWO4 disordered solid solution, J. Solid State Chem. 258 (2018) 146–155. doi:10.1016/j.jssc.2017.10.014.

[21] A. Hallaoui, A. Taoufyq, M. Arab, B. Bakiz, A. Benlhachemi, L. Bazzi, J.C. Valmalette, S. Villain, F. Guinneton, J.R. Gavarri, Structural, vibrational and photoluminescence properties of Sr(1-x)PbxMoO4 solid solution synthesized by solid state reaction, Mater. Res. Bull. 79 (2016) 121–132. doi:10.1016/j.materresbull.2016.03.015.

[22] F. Xue, H. Li, Y. Zhu, S. Xiong, X. Zhang, T. Wang, X. Liang, Y. Qian, Solvothermal synthesis and photoluminescence properties of BiPO4 nano-cocoons and nanorods with different phases, J. Solid State Chem. 182 (2009) 1396–1400. doi:10.1016/j.jssc.2009.02.031.

[23] G. Du, X. Kan, Y. Han, Z. Sun, W. Guo, Structure and luminescence of YPO4:Dy3+ microflowers, Mater. Lett. 74 (2012) 229–231. doi:10.1016/j.matlet.2012.01.117.

[24] J. Yang, H. Xiong, J. Dong, C. Yang, S. Gan, L. Zou, Facile hydrothermal synthesis and luminescent properties of $Sm^{3+}/Eu^{3+}$ codoped GdPO<inf>4</inf> phosphors, J. Phys. Chem. Solids. 111 (2017) 355–363. doi:10.1016/j.jpcs.2017.08.031.

[25] M. Kirubanithy, A.A. Irudayaraj, A.D. Raj, S. Manikandan, Synthesis, Characterization and Photoluminescence Behaviours of CePO4 and Tb-doped CePO4 Nanostructures, Mater. Today Proc. 2 (2015) 4344–4347. doi:10.1016/j.matpr.2015.10.024.

[26] W. Zhang, Y. Ni, W. Huang, C. Lu, Z. Xu, Hydrothermal synthesis, structure study and luminescent properties of YbPO4:Tb3+ nanoparticles, J. Rare Earths. 28 (2010) 299–302. doi:10.1016/S1002-0721(10)60337-7.

[27] G. Bühler, C. Feldmann, Microwave-assisted synthesis of luminescent LaPO4:Ce,Tb nanocrystals in ionic liquids, Angew. Chemie - Int. Ed. 45 (2006) 4864–4867. doi:10.1002/anie.200600244.

[28] A. Bouddouch, E. Amaterz, R. Haounati, Y. Naciri, A. Taoufyq, B. Bakiz, F. Guinneton, S. Villain, J.-R. Gavarri, A. Benlhachemi, Synthesis , characterization and luminescence properties of manganese phosphate Mn3(PO4)2, Mater. Today Proc. 3 (2019) 2–7. doi:10.1016/j.matpr.2019.08.058.

[29] A. Hallaoui, A. Taoufyq, M. Arab, B. Bakiz, A. Benlhachemi, L. Bazzi, S. Villain, J.C. Valmalette, F. Guinneton, J.R. Gavarri, Influence of chemical substitution on the photoluminescence of Sr(1-x)PbxWO4 solid solution, J. Solid State Chem. 227 (2015) 186–195. doi:10.1016/j.jssc.2015.04.004.

[30] B. Chandra Babu, G.G. Wang, A.P. Baker, B.L. Wang, Synthesis, photoluminescence, energy transfer and thermal stability of SmPO4@SiO2:Eu3+ core-shell structured red phosphors for WLEDs, J. Alloys Compd. 766 (2018) 74–87. doi:10.1016/j.jallcom.2018.06.256.

[31] J.M. Heuser, R.I. Palomares, J.D. Bauer, M.J.L. Rodriguez, J. Cooper, M. Lang, A.C. Scheinost, H. Schlenz, B. Winkler, D. Bosbach, S. Neumeier, G. Deissmann, Structural characterization of (Sm,Tb)PO4 solid solutions and pressure-induced phase transitions, J. Eur. Ceram. Soc. 38 (2018) 4070–4081. doi:10.1016/j.jeurceramsoc.2018.04.030.

[32] Z. Wu, Z. Huang, G. Yin, L. Wang, F. Gao, Fabrication of Gd/Eu-codoped SmPO4 nanorods for dual-modal magnetic resonance and bio-optical imaging, J. Colloid Interface Sci. 466 (2016) 1–11. doi:10.1016/j.jcis.2015.10.048.

[33] D. Kashiwagi, A. Takai, T. Takubo, H. Yamada, T. Inoue, K. Nagaoka, Y. Takita, Catalytic activity of rare earth phosphates for SF6 decomposition and promotion effects of rare earths added into AlPO4, J. Colloid Interface Sci. 332 (2009) 136–144. doi:10.1016/j.jcis.2008.12.003.

[34] L. He, J. Xu, T. Han, H. Han, Y. Wang, J. Yang, J. Wang, W. Zhu, C. Zhang, Y. Zhang, SmPO 4 -coated Li 1.2 Mn 0.54 Ni 0.13 Co 0.13 O 2 as a cathode material with enhanced cycling stability for lithium ion batteries, Ceram. Int. 43 (2017) 5267–5273. doi:10.1016/j.ceramint.2017.01.052.

[35] D.F. Mullica, D.A. Grossie, L.A. Boatner, Coordination geometry and structural determinations of SmPO4,EuPO4 and GdPO4, Inorganica Chim. Acta. 109 (1985) 105–110. doi:10.1016/S0020-

1693(00)84549-1.

[36] K. Popa, R.J.M. Konings, High-temperature heat capacities of EuPO4 and SmPO4 synthetic monazites, Thermochim. Acta. 445 (2006) 49–52. doi:10.1016/j.tca.2006.03.023.

[37] Y. HIKICHI, Synthesis of monazite (RPO4, R=La, Ce, Nd, or Sm) by solid state reaction., Mineral. J. 15 (1991) 268–275. doi:10.2465/minerj.15.268.

[38] J.G. Pepin, E.R. Vance, Crystal data for rare earth orthophosphates of the monazite structure-type, J. Inorg. Nucl. Chem. 43 (1981) 2807–2809. doi:10.1016/0022-1902(81)80621-5.

[39] K.S. Gavrichev, V.M. Gurevich, M.A. Ryumin, A. V. Tyurin, L.N. Komissarova, Heat capacity and thermodynamic functions of SmPO4 at 10–1600 K, Geochemistry Int. 53 (2015) 607–616. doi:10.1134/s0016702915070046.

[40] I. V. Kityk, M. Nyk, W. Strek, J.M. Jablonski, J. Misiewicz, Circularly photostimulated electrogyration in europium-and terbium-doped GaN nanocrystals embedded in a silica xerogel matrix, J. Phys. Condens. Matter. 17 (2005) 5235–5245. doi:10.1088/0953-8984/17/34/008.

[41] G.M. Begun, G.W. Beall, L.A. Boatner, W.J. Gregor, Raman spectra of the rare earth orthophosphates, J. Raman Spectrosc. 11 (1981) 273–278. doi:10.1002/jrs.1250130315.

[42] L.Y. Yang, S.Y. Dong, J.H. Sun, J.L. Feng, Q.H. Wu, S.P. Sun, Microwave-assisted preparation, characterization and photocatalytic properties of a dumbbell-shaped ZnO photocatalyst, J. Hazard. Mater. 179 (2010) 438–443. doi:10.1016/j.jhazmat.2010.03.023.

[43] H.J. Lee, J.U. Park, S. Choi, J. Son, M. Oh, Synthesis and photoluminescence properties of Eu 3+ -doped silica@coordination polymer core-shell structures and their calcinated silica@Gd 2 O 3 :Eu and hollow Gd 2 O 3 :Eu microsphere products, Small. 9 (2013) 561–569. doi:10.1002/smll.201200558.

[44] K.Y. Jung, Y.C. Kang, Y.K. Park, DMF effect on the morphology and the luminescence properties of Y2O3:Eu3+ red phosphor prepared by spray pyrolysis, J. Ind. Eng. Chem. 14 (2008) 224–229. doi:10.1016/j.jiec.2007.09.011.

[45] X. xiao Wang, Y. lun Xian, G. Wang, J. xin Shi, Q. Su, M. lian Gong, Luminescence investigation of Eu3+-Sm3+ co-doped Gd2-x-yEuxSmy(MoO4)3 phosphors as red phosphors for UV InGaN-based light-emitting diode, Opt. Mater. (Amst). 30 (2007) 521–526. doi:10.1016/j.optmat.2007.01.006.

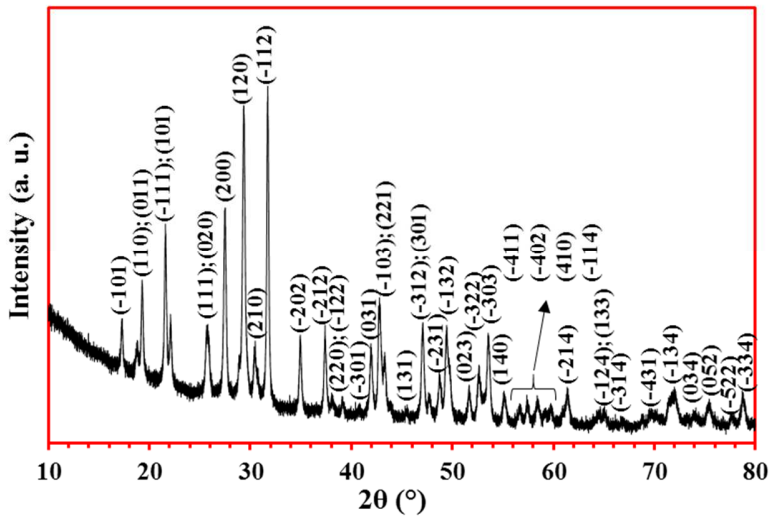


Fig. 1. XRD pattern of samarium phosphate $SmPO_4$ calcined at 900 °C.

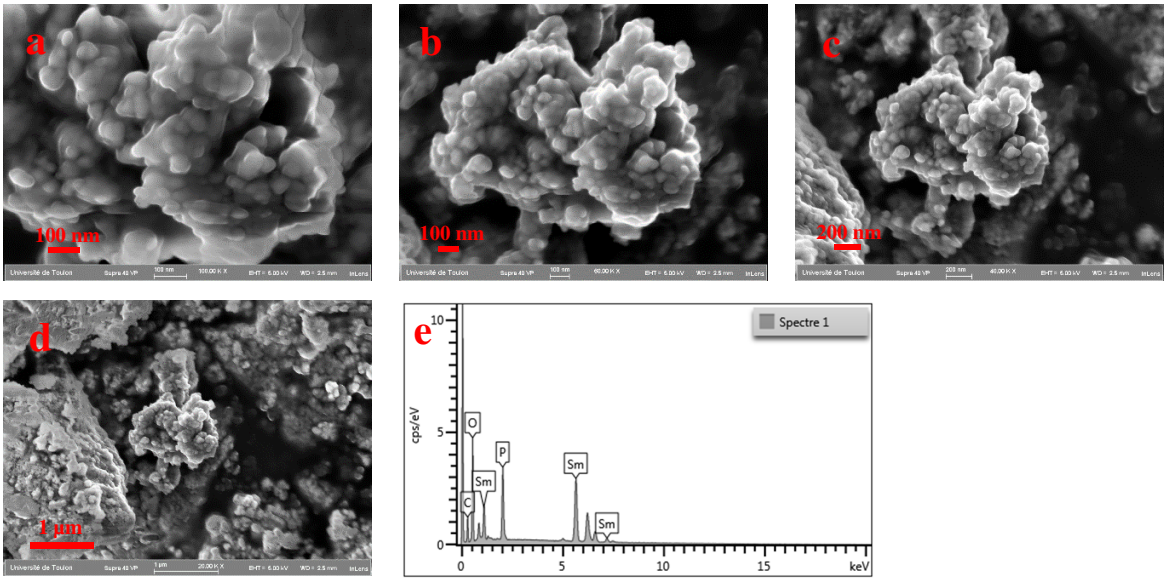


Fig. 2. SEM images and EDX spectrum of samarium phosphate $SmPO_4$ treated at 900 °C.

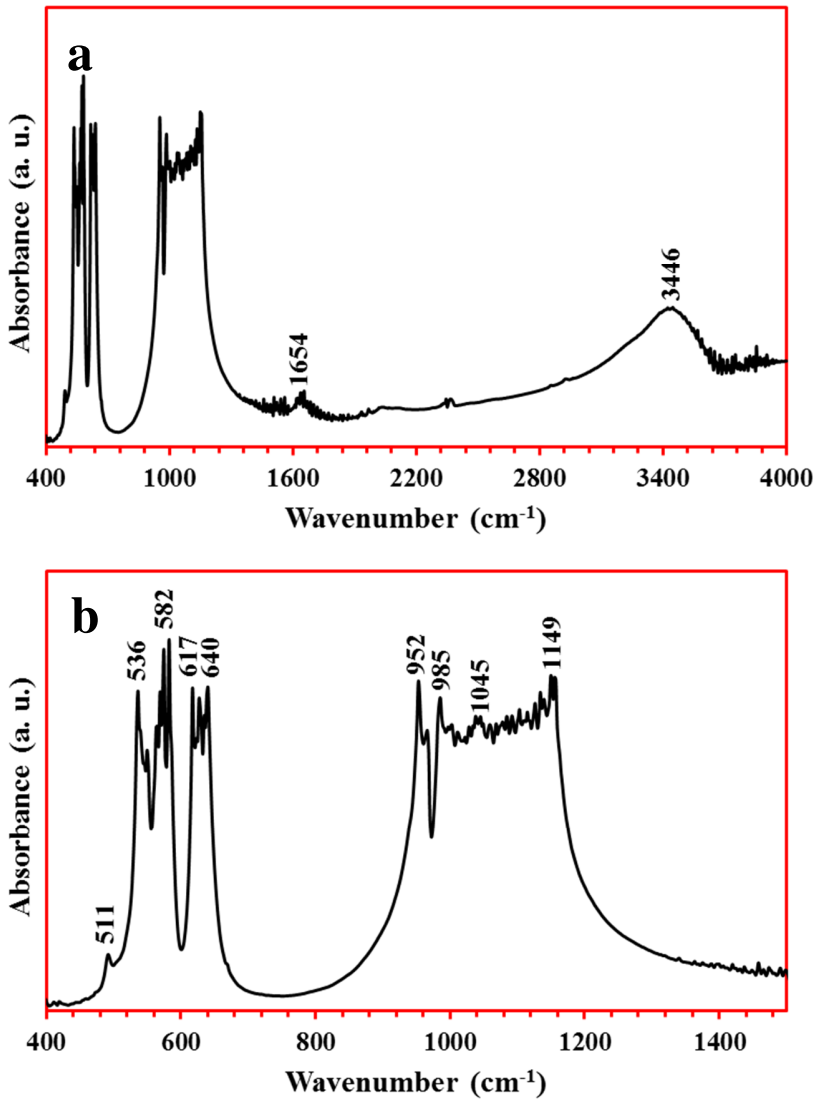


Fig. 3. FTIR spectrum of $SmPO_4$ nanoparticle between (a) 400-4000 and (b) 400-1400 $cm^{-1}$.

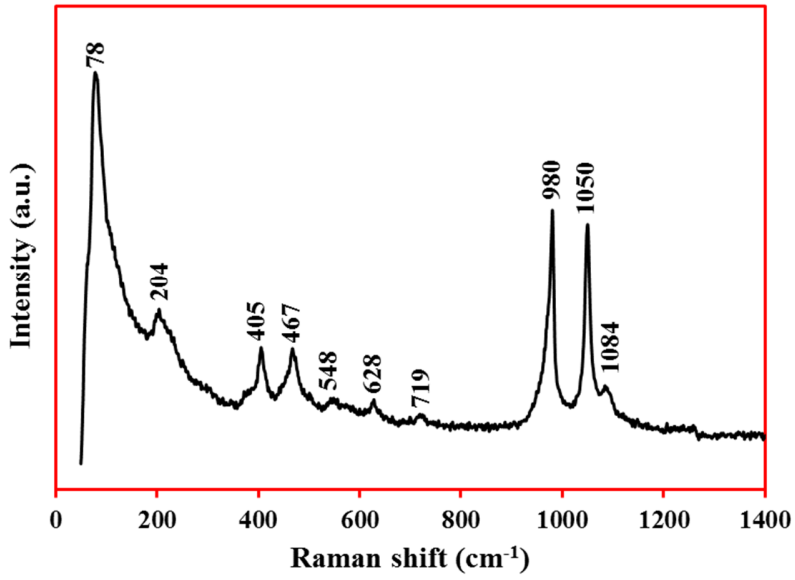

Fig. 4. Raman spectrum of $SmPO_4$ sample.

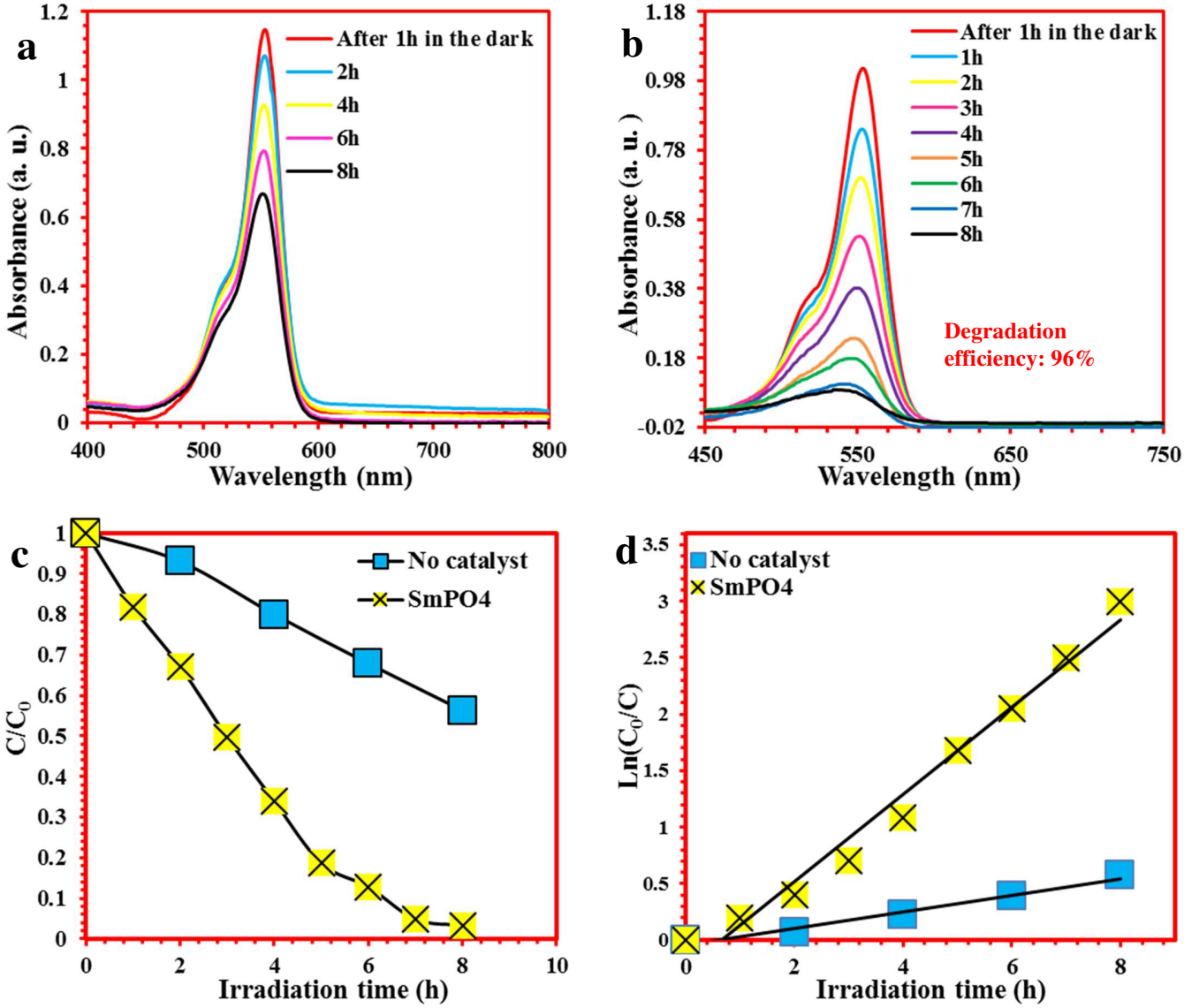


Fig. 5. (a) stability of the rhodamine B under UV light, (b) UV–vis absorption with time irradiation of a solution containing 100 mg $SmPO_4$ and a 5ppm of rhodamine B, (c) Photodegradation of RhB in SmP suspension under UV-visible light (initial concentration of RhB, 5 mg/L). (d) pseudo-first-order kinetics of the photocatalyst.

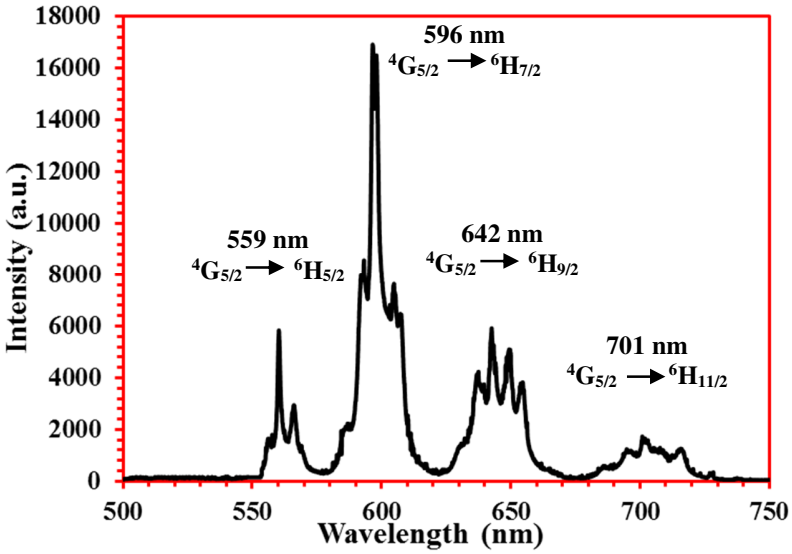


Fig. 6. Experimental emission bands of the $SmPO_4$ polycrystalline phase.

Table 1. Refined cell parameters and cell volumes of samarium phosphate crystal lattice.

| **Chemical formula** | $SmPO_4$ |
|---|---|
| **a (Å)** | 6.6750±0.0016 |
| **b (Å)** | 6.8831±0.0015 |
| **c (Å)** | 6.3601±0.0017 |
| **β (°)** | 103.85±0.02 |
| **Volume ($Å^3$)** | 283.72±0.20 |
| **Density μ ($g.cm^{-3}$)** | 5.74 |